Looking inside electrodes at the microscale with LIBS : Li distribution

Jordan Fernandes, Loïc Sorbier, Sylvain Hermelin, Jean-Michel Benoit, Christophe Dujardin, Charles-Philippe Lienemann, Julien Bernard, Vincent Motto-Ros

Spectrochimica Acta Part B: Atomic Spectroscopy 221 (2024) 107047

Contents lists available at ScienceDirect

Spectrochimica Acta Part B: Atomic Spectroscopy

journal homepage: www.elsevier.com/locate/sab

Looking inside electrodes at the microscale with LIBS: Li distribution

Jordan Fernandes [a,b], Loïc Sorbier [b], Sylvain Hermelin [a], Jean-Michel Benoit [a], Christophe Dujardin [a,c], Charles-Philippe Lienemann [b], Julien Bernard [b], Vincent Motto-Ros [a,*]

[a] Institut Lumière Matière UMR5306, Université Lyon 1 – CNRS, Université de Lyon, 69622 Villeurbanne, France
[b] IFP Energies Nouvelles, Rond-Point de l'échangeur de Solaize, BP 3, 69360 Solaize, France
[c] Institut universitaire de France (IUF), 1 rue Descartes, 75231 PARIS CEDEX 05, France

ARTICLE INFO

Keywords:
Micro LIBS imaging
Micrometer scale resolution
Lithium
Electrodes

ABSTRACT

The enhancement of Lithium-ion batteries (capacity, power, life span, etc.) poses a significant challenge in the pursuit of decarbonizing individual modes of transportation. The behavior and performance of these batteries vary primarily based on the nature of their electrode materials, with some still undergoing development. To gain a deeper understanding of the aging mechanisms that occur during battery operation, it is essential to assess the distribution of lithium within the electrodes with the highest possible spatial resolution. In this study, we showcase the application of micro-LIBS imaging as a multi-elemental characterization tool for investigating the aging mechanisms. By employing a high numerical aperture (0.42) microscope objective and a short wavelength laser (266 nm), we have developed a high lateral resolution micro-LIBS imaging experimental device approaching 2 μm. Performance evaluation was conducted on a certified aluminum sample with a high silicon content (~18 %). The utility of this new micro-LIBS instrumentation in studying Nickel Manganese Cobalt (NMC) batteries, revealing the formation of preferential sites for inactive lithium in negative electrodes, is also demonstrated.

1. Introduction

Lithium-ion (Li-ion) batteries have become indispensable for powering portable electronic devices. Concurrently, as European governments initiatives intensify to curtail CO_2 emissions (European green pact), the evolution of electric vehicles is an ongoing endeavor [1]. To facilitate the widespread adoption of electric cars necessitates continual enhancements in their performance and safety. An essential means of achieving such advances lies in the comprehensive characterization of Li-ion batteries for modeling validation, particularly the electrodes constituting their core components [2]. The investigation of aging phenomena at the electrode scale, whether positive or negative, emerges as a distinct and imperative research focus. The principal aging phenomenon within Li-ion batteries is identified as Solid Electrolyte Interphase (SEI) growth [3–5]. Starting from the inaugural charge cycle, a subset of lithium ions undergoes a reduction reaction of the electrolyte when in contact with an electrode possessing a potential less than 1 V vs. Li/Li^+. A permeable lithium ions passive layer is then formed in contact with the negative electrode. The evolution of this layer is mandatory for the utilization of low-potential electrodes, such as graphite. However, across successive charge/discharge cycles, the SEI layer undergoes continual expansion resulting in a progressively entrapping more and more cyclable lithium (known as LLI for Loss of Lithium Inventory). This growth of a non-conductive SEI layer can also lead to the electrical insulation of some graphite particles in the composite electrode, which is one of the phenomena responsible for the loss of capacity of the electrode (known as LAM for Loss of Active Material). Insulated active material particles are in more or less lithiated states, and therefore also trap some of the lithium cyclable (LLI) within them. Consequently, a gradual diminishment in the internal capacity of the battery ensues. Furthermore, the layer imposes a hindrance on the transfer of lithium ions, resulting in a gradual escalation of the system's internal resistance. Under specific operational conditions, such as fast charging or low temperatures, the occurrence of lithium plating is noteworthy. This phenomenon involves the deposition of lithium in metallic form on the negative electrode's surface [6]. While this process is largely reversible during discharge, it contributes to the formation of a SEI, which, contingent upon the morphology of the lithium deposits, may gradually isolate metallic lithium particles from the electrode's electronic percolation network (referred to as "dead lithium"). Aside from safety

* Corresponding author.
E-mail address: vincent.motto-ros@univ-lyon1.fr (V. Motto-Ros).

https://doi.org/10.1016/j.sab.2024.107047
Received 1 February 2024; Received in revised form 19 June 2024; Accepted 11 September 2024
Available online 12 September 2024

concerns arising from the formation of lithium dendrites, this phenomenon gives rise to a substantial LLI and therefore a loss in capacity [7]. The main consequence of all the aging phenomena mentioned above is therefore the trapping of cyclable lithium in various forms: in the SEI layer, in metallic form on the surface of the electrodes, or intercalated in the grains of materials that have become inactive.

To reduce research costs and development, various electrochemical models have been devised, including the pseudo 2D (P2D) model [8,9]. This model delineates each point on the electrode as a spherical particle representing the grains of active material. The study encompasses two dimensions, employing parameters such as the radius of the grains of active material and the thickness of the electrode (mean size positive and negative active matter grain of electrodes is ~5 μm [8]). Aging mechanism modeling consists of modeling each of the aging mechanisms mentioned above such as SEI growth, and adding them to the set of equations of the P2D model [10,11]. However, the application of this model necessitates knowledge of many parameters (at least 30 parameters) associated with Li-ion batteries (e.g., mean particle radius, porosity, lithium concentration, activation rate, etc.) [8]. The research for these parameters is often laborious and demands tailoring to the specific battery under investigation. While certain variables may be taken from literature, others require direct measurement, with some, like the quantitative distribution of lithium in the positive/negative electrodes, posing challenges. The quantification and imaging of lithium at the required spatial resolution presents difficulties using conventional techniques due to its low weight. SEM-EDS (Scanning Electron Microscopy - Energy Dispersive Spectroscopy) has gained popularity in battery characterization due to its ability to analyze various elements of interest (with $Z > 3$) at low spatial resolution (~μm) [8,12]. Nevertheless, its limitation in detecting low lithium content in a sample constitutes a primary drawback for this study. Presently, EDS detectors have a lithium detection and quantification limit of approximately 20 wt% [13,14]. While X-ray imaging exhibits higher spatial resolution compared to SEM-EDS (~30 nm), it facilitates both in-situ and ex-situ investigations of a battery [15].

Laser-Induced Breakdown Spectroscopy (LIBS) stands out as a remarkably sensitive technique for lithium monitoring. This method has been effectively employed to characterize the elemental distribution of many elements including lithium within diverse positive [16,17] and negative [18,19] electrodes. To the best of our knowledge, the most advanced spatial resolution achieved by a LIBS system dedicated to lithium elemental mapping in the context of Li-ion battery studying is 38 μm, as demonstrated on a solid electrolyte [20]. In the pursuit of studying aging phenomena at the electrode level with microscopic precision, it becomes imperative to enhance the spatial resolution of the LIBS technique to the micrometer and even targeting the sub micrometer range. Several investigations have been conducted to develop femtosecond (fs)-LIBS [21–23] and nanosecond (ns)-LIBS [24,25] systems, incorporating large numerical aperture microscope objectives to achieve spatial resolutions in the micrometer to sub-micrometer range. This refined resolution facilitates the in-depth study of lithium distribution at the microscopic scale. In micro-LIBS imaging, the spatial resolution is contingent upon the distance between two successive craters, and reaching smaller craters allows to reduce the measurement pitch. The dimensions of these craters are fundamentally influenced by the combination of the laser energy and the size of the laser beam at focus on the analyzed sample. The literature attests that ultraviolet (UV) lasers offer enhanced reproducibility and the formation of smaller craters due to the lower diffraction limit of the laser beam [26]. However, UV lasers typically exhibit generally a multimode beam profile with an M^2 value of about 2 or above, thereby compromising the achievable focusing power. Consequently, the focusing apparatus must be equipped with an optical instrument capable of correcting the laser beam profile to a (close-to) Gaussian beam, ensuring optimal performance in term of focalization.

In this study, we introduce a novel micro-Laser-Induced Breakdown Spectroscopy (micro-LIBS) imaging apparatus designed to attain micrometer-scale spatial resolution. This device employs a microscope objective with high numerical aperture and a UV ns laser, thereby achieving an outstanding lateral resolution of 2 μm. The capability of this system extends to generating elemental maps, specifically of lithium, along with other pertinent elements, within diverse electrodes undergoing distinct lithiation states. The experimental configuration of the apparatus will be described, accompanied by a presentation of illustrative examples obtained from various electrode types.

2. Experimental methods

2.1. Samples

This study involved the analysis of three samples, a certified aluminum reference (MBH-54× GS20J1 E), internal components from a commercial disassembled Li-ion battery cell (NMC811/Graphite pouch type), and pristine Li-ion positive electrodes mounted and cycled in half cell configuration. The aluminum sample was composed mainly by aluminum (80.7±0.5 %), silicon (18.8 ±0.5 %), copper (0.308 ±0.009 %) and magnesium (0.186 ± 0.003 %). Li-ion batteries sample preparation was performed in our laboratory and is the same for both electrodes. Both battery samples were initially disassembled and rinsed of its electrolyte under argon atmosphere. From the first battery sample (Fig. 1.a) a stack of positive, separator and negative electrodes originating from commercial battery scrap were fixed in an epoxy resin. The battery being in the discharged state, Li will be mainly present in the positive electrode. Due to the lack of information concerning this sample, the exact number of cycle and the exact stoichiometry is unknown for this sample. The second battery sample (Fig. 1.b) is composed by NMC 811 electrodes. Coin cells with pristine electrodes (Customcells NMC811) were mounted for the purpose of this work in half-cell configurations versus lithium metal foils with electrolyte composed by 1 M $LiPF_6$ in EC/DMC (1/1 wt.) (Ethylene Carbonate / DiMethylCarbonate) mixture doped with 1 % wt. vinylene carbonate, imbibed in a glass fiber (Whatman GF/D) separator. The half-cells were formed and then placed at different state of charge (SOC): 0 %, 50 % and 100 % experiencing only one full cycle of charge and discharge at ambient temperature. The capacity window is defined by the potential limits of the system according to the datasheet: $U_{min} = 3$ V vs. Li/Li^+ and $U_{max} = 4.3$ V vs. Li/Li^+. The electrodes thus obtained have different lithium intercalation states (x_{Li}): SoC 0 %: $x_{Li} \sim 0.95$, SoC 50 %: $x_{Li} \sim 0.59$ and SoC 100 %: $x_{Li} \sim 0.27$ estimated from the number of exchanged electrons and the mass of active material. Once these states were achieved, we included after dismantling only the positive electrodes in the epoxy resin in ambient air. The use of epoxy resin improves the analysis conditions by solidifying the sample and allows achieving a mirror-like polishing of the electrode cross sections, which is required to have a full control on the focal point. Both epoxy-mounted samples were polished with SiC abrasive sheets lubricated by heptane solvent under ambient air condition. They were stored in moisture-free boxes before LIBS imaging.

2.2. LIBS instrumentation

2.2.1. General overview

The experimental setup is schematically depicted in Fig. 2.a. It consists of a Q-switched, fourth-harmonic Nd:YAG UV laser at 266 nm (Q-smart 450, Lumibird) with an energy of 50 mJ, and operating at a repetition rate of 20 Hz with a pulse duration of 5 ns. This repetition rate allows for the creation of 72,000-pixel maps in 1 h. The laser beam is directed to the microscope lens using mirrors (NB1-K04, Thorlabs) selected to match the laser's wavelength. The modification of the laser energy is ensured by a tandem of computer-controlled attenuators (Altechna Power XP, ATT266 Quantum Composer), allowing an accurate control of the laser energy. Then, the laser beam goes through a beam shaping system, described more precisely below. The goal of this device is to improve the quality factor M^2 of laser beam. The laser beam

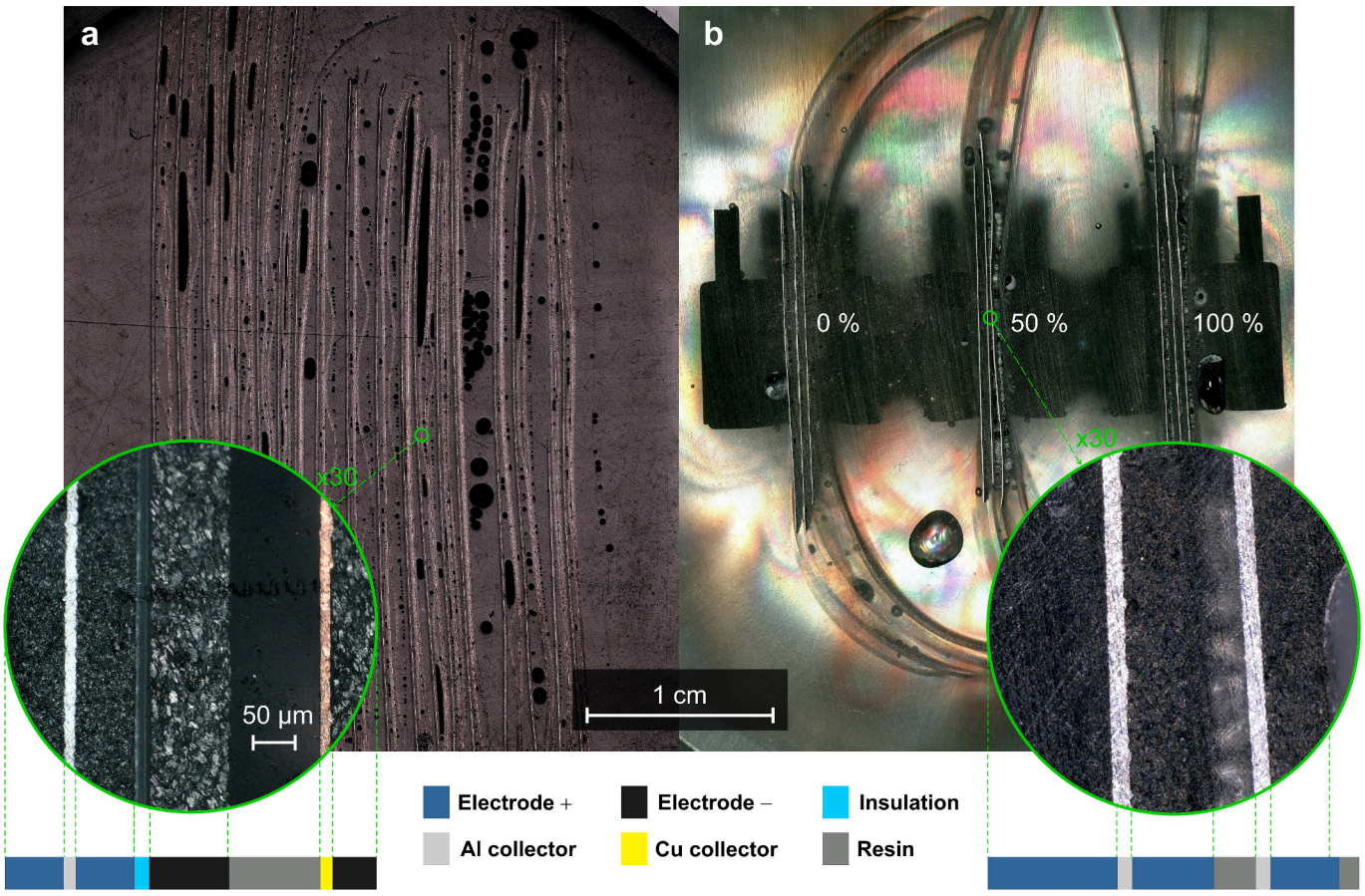

Fig. 1. (a) Optical image of the sample composed of NMC-type battery. (b) Optical image of the sample composed of NMC 811-type electrodes at SoC 0, 50 and 100 %.

is finally redirected by a dichroic mirror (DM) and focused on the sample surface by a × 50 microscope lens (LMUL-50×-UVB, Thorlabs). This microscope objective has an entrance pupil diameter of 3.4 mm, a focal length of 4 mm (0.42 numerical aperture), and a working distance of 12 mm. This objective has an optical design chromatically optimized in the UV wavelength range, from 240 to 360 nm. The used dichroic mirror (DM) reflected every wavelength below 400 nm and transmitted all wavelengths above. Its utilization is necessary to observe the image of the sample surface through the objective lens, and adjust accurately the objective to sample distance. To this aim, we used a Thorlabs LED at 405 nm (M405L4) coupled with a monochrome CMOS camera (CS165MU, Thorlabs). Despite the wavelength of the LED being outside the nominal optical range of the microscope objective, it is still possible to visualize a sharp image at the focal position, and use this image to accurately control the objective-to-sample surface position. A typical image recorded with this monitoring camera is shown in Fig. 2.c, which corresponds to a crater formed on a steel sample. An argon flow of 0.7 L/min directed at the plasma region was used both to prevent surface contamination due to ablated material deposition from previous laser shots and to enhance the emission signal collection. The diameter and the distance from the plasma of the nozzle was respectively 2 mm and ~ 8 mm.

2.2.2. *Beam shaping system*

To achieve the smallest possible laser beam size at the microscope objective focal plane, a beam shaping system is used to correct the original laser beam profile ($M^2 \sim 2$) into a quasi-Gaussian beam profile ($M^2 \sim 1$). This system is shown in Fig. 2.b and includes a circular pinhole of 50 µm of diameter (metal-wire drawing dies made of diamond, from Balloffet). This circular aperture induces an Airy disk following the Fraunhofer diffraction pattern. The intensity profile of the central lobe of this diffraction pattern is very similar to a Gaussian profile [25,27]. To use only the central diffraction lobe, a collimation lens and a diaphragm was employed to project the pinhole image to infinity with the same diameter as the microscope objective's entrance pupil. This lens was chosen with a focal length of 50 cm for a 50 µm aperture pinhole. According to our calculations and experiments, a lateral resolution of less than 2 µm can be achieved in this configuration. However, using such a small-diameter circular aperture leads to a consequent loss of fluence at its output. To compensate for this loss, we used a beam expander ×2 (BE02–532) mounted in a reverse configuration, reducing the laser beam diameter by 2 and increasing laser fluence by about 4 at the pinhole output. For information, the typical energy at the entrance of the pinhole was ~30 mJ, while ~3.5 µJ was obtained at the output. With the used attenuators it was then possible to work with a typical energy comprised between few hundreds of nanoJoules and ~ 2.1 µJ, values measured at the ×50 objective lens output.

2.2.3. *Spectral detection*

The spectral detection was ensured by two Czerny-Turner spectrometers with ICCD cameras. The first spectrometer was optimized to work in the UV region (Shamrock 500i, iStar ICCD gen2, Andor technology). It was used principally to detect the aluminum and copper intense UV lines (typical range used: 300–388 nm). The second spectrometer (Kymera 328i, iStar ICCD gen3, Andor technology) was configured for the detection of intense lithium lines present the visible range (610.353 and 670.791 nm lines). To maximize the light collection, we used two aspheric lenses, both of 10 mm focal lengths. The first one was coated for UV spectral range (245–420 nm) and was dedicated to spectrometer 1, and the other was coated for the visible and NIR region

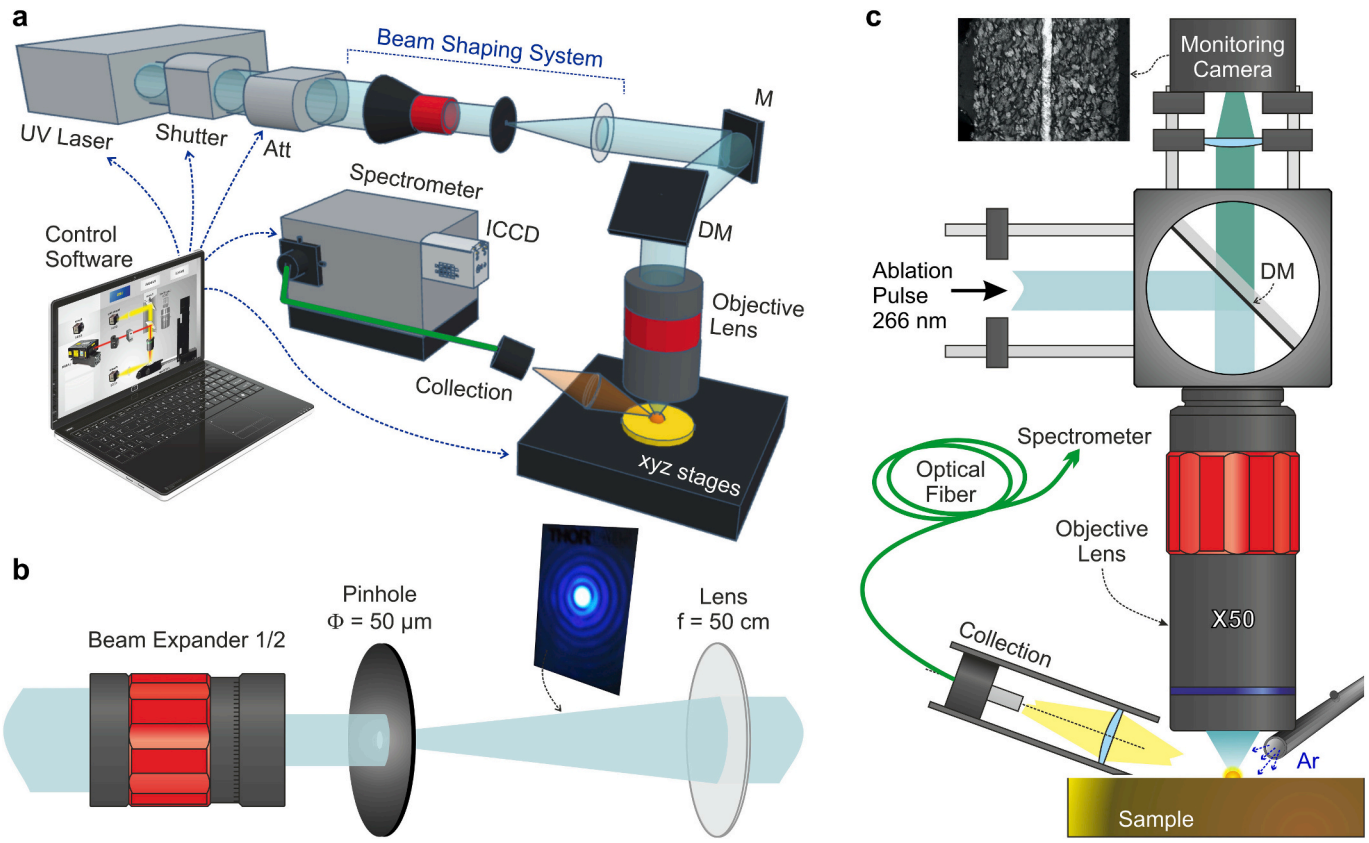

Fig. 2. (a) Working schema of the experimental device. (b) Principle of the beam shaping system. (c) Zoom of the objective part of the experimental device.

(650–1050 nm) for spectrometer 2. For each of the two collection systems, a circular to linear fiber bundle constituted of 19 optical fibers of 100 µm core diameter was used to couple the light to the spectrometers. The first spectrometer was equipped with a 600 l/mm grating blazed at 300 nm. The typical slit aperture used was 50 µm. In this configuration, we were able to detect the range between 300 and 388 nm with a resolution of ~0.2 nm. The second spectrometer was composed by a 600 l/mm blazed at 600 nm. With this equipment we were able to detect emission lines in a range of 600 to 688 nm with a resolution of ~0.3 nm. Both detectors were synchronized to the laser Q-switch trigger (see below for more details). The delay and gate were, 95 ns and 1 µs for the first spectrometer, and 0 ns and 1 µs for the second, respectively.

2.2.4. *Movements and triggering*

Finally, the sample was placed on a motorized XYZ translation stages (M-403-2PD, PI), allowing movement in each direction up to a distance of 50 mm at a maximum speed of 10 mm/s. Such stages have minimum incremental motion of 0.25 µm and repeatability of 1 µm. Homemade software developed in the LabVIEW environment controlled the entire system and allowed the use of automated sequences to scan the region of interest.

Time control of the various instrumental devices has been optimized to reduce possible jitters and latency. To guaranty the best laser energy stability, the laser was fired continuously and the shutter was used to control the delivery of laser pulses to the sample surface. During a scanning sequence, a shutter was closed between each line change. The opening and closing of the shutter were controlled by a delay box triggered by the laser's flash lamp. This delay box allowed to open the shutter for a duration corresponding to a controlled number of pulses. Compared to usual LIBS analysis, when working with low energy pulses, the plasma lifetime is drastically decreased, with a full duration in the hundreds of ns scale (c.f. section 3.2). Due to the internal latency of ~50 ns of the ICCD camera used, detectors were triggered with a homemade comparator using the shutter and the external laser trigger signals. This process allowed a perfect control on the triggering system, leading to the recording of the entire plasma emission.

2.3. *LIBS data processing*

The general protocol used for the construction of the elemental images has been described in several papers [28,29]. Briefly, the line intensities (associated with the elements of interest) were retrieved for each sample position (i.e. spectrum) by defining a baseline on a spectral range of a few nanometers and subtracting it from the emission line of interest [30]. Therefore, this procedure involves the selection of two spectral ranges—one dedicated to the retrieval of emission line intensity and the other focused on estimating the spectrum background. Mathematically, the extracted intensity I_s may be expressed as follows:

$$I_s = \sum_{i=1}^{n_s} I_i - n_s \overline{I_{BG}}$$

Where, I_i represents the spectrum intensity at the wavelength index i, n_s the number of spectral channels in the line range, $\overline{I_{BG}}$ the average intensity of the background range (composed by n_{bg} values). This methodology offers two principal advantages. Firstly, given the large number of spectra under consideration, expeditious processing is imperative for generating extensive elemental images. The computational efficiency of this approach is notably high, with the capacity to handle ~100,000 spectra per second. Secondly, it mitigates noise and increase the robustness to a significant extent, compared to more conventional extraction methods.

For each selected line, the retrieved 2D matrix, containing spatial and spectral information, was saved in .txt format, and ImageJ software (National Institutes of Health, USA) was used to apply a false color scale to present a visual result in the form of elemental images.

3. Results

While the main focus of this article is on imaging the distribution of lithium at the micrometer scale in battery electrodes, we first conducted a study on a reference aluminum sample to assess the achievable performance in term of resolution with the proposed instrumentation. Due to the inherently porous and heterogeneous nature of the electrodes, it was not possible to evaluate crater size or plasma kinetic properties on this type of sample. Therefore, a preliminary study was conducted on a reference aluminum sample to assess the influence of energy on crater size and plasma lifetime, and more generally, to evaluate our instrument for micro-analysis purposes.

3.1. Reference aluminum sample

3.1.1. Crater morphology

The examination of crater size post-ablation is mandatory for assessing the imaging device's performance. To characterize these craters, laser shots were executed on the surface of a mirror-polished aluminum sample spaced at 30 μm intervals. Ultimately, 100 laser shots at six different laser energies were conducted to observe the crater morphology and reproducibility. The selected energies for the study were $E_1 = 156$ nJ, $E_2 = 208$ nJ, $E_3 = 522$ nJ, $E_4 = 618$ nJ, $E_5 = 882$ nJ and $E_6 = 1.23$ μJ (values measured at the microscope lens output). The choice of aluminum as the sample was made in accordance with the composition of Li-ion batteries. Specifically, the positive electrode collectors are predominantly composed of aluminum, while the majority of negative electrodes utilized consist of copper. Given that aluminum has a lower ablation threshold than copper [31], resulting craters on its surface are larger. Consequently, the optimal value obtained for aluminum may be also applicable to copper.

The diameters of the craters formed on the aluminum sample at 6 laser pulse energies are depicted and scaled in Fig. 3.a. It is evident that the formed craters exhibit a predominantly circular shape, crediting the efficiency of the beam shaping described in Section 2.2. Craters generated with this profile exhibit a characteristic depth at their centers. Furthermore, it is observed that increasing the laser energy results in an augmented diameter of the surface-formed craters, as illustrated in Fig. 3.a. The crater diameter measurement was made at the top periphery of the crater formation. The diameter values showed in Fig. 3.b represents the mean size of 10 different craters made at same laser energy. For the lowest energy (E_1), the crater diameter formed at the surface was 1.2 μm. Considering the FWHM of the measured craters, one may anticipate possible sub-micrometric spatial resolution with a small cross talk between adjacent pixels. Upon increasing the energy to 1.23 μJ, the crater size significantly expands, with an average diameter of 3.1 μm.

Crater depth was measured by an optical microscope and are represented in Fig. 3.c. Each point in this figure represents the mean value of 10 crater depths for one laser energy. Although the accuracy of the measurement is questionable, it provides a reasonable estimate of the crater depth and its evolution with regard to the energy. In this figure, we observe a linear behavior (in the energy explored range) in the crater depth along the laser energy, indicating a consistent ablation regime. Furthermore, we note that the depth of the crater is substantially correlated to its diameter. At low energy, we determined a mean depth of 3.6 μm for a diameter of 1.2 μm, and at the highest energy level, the depth is 8.5 μm for a diameter of 3.3 μm. On average, the crater depth is twice the diameter. The estimation of the ablated mass, based on a conical crater shape assumption, results in extremely low ablated material mass: 4 and 66 picograms for the lowest and highest energy, respectively.

The variation of the signal-to-noise ratio (SNR) along laser energy was also studied and is depicted in supplementary fig. 1. To compare the intensity of emitted lines, the average of 100 laser shots on the sample surface was calculated. Additionally, the average emission spectra between 600 and 680 nm obtained on electrode films and for different laser energies are presented in Fig. 3.d. At low laser energy levels, the SNR starts to decrease, particularly in the case of aluminum, where it has a value of 20, indicating some difficulty in working at this low energy. For lithium, measured on an electrode film, the SNR is above 50 for the same laser energy. If we observe the emission spectra associated at this laser energy, we clearly see both emission lines of lithium. These lines exhibit an intensity significantly higher than the neighboring noise, indicating the feasibility of elemental imaging with the smallest achievable crater size for Li-ion electrodes. Thus, all the elemental maps

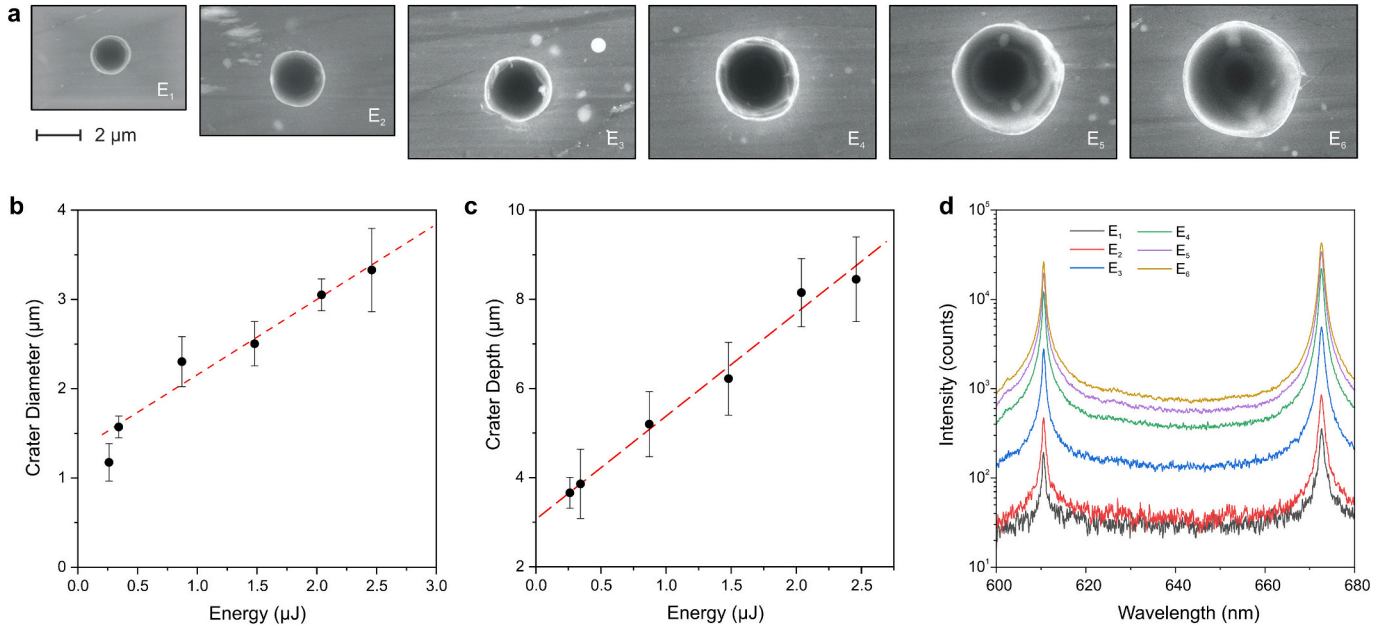

Fig. 3. (a) SEM imaging of craters made in aluminum sample with different energies ($E_1 = 156$ nJ, $E_2 = 208$ nJ, $E_3 = 522$ nJ, $E_4 = 618$ nJ, $E_5 = 882$ nJ and $E_6 = 1.23$ μJ). (b) Evolution of the diameter of the crater along laser energy. (c) Evolution of the crater depth along laser energy. (d) Mean spectra with background correction obtained with 100 laser shots in an NMC 811 electrode for the different laser pulse energies.

presented below were produced with a laser energy of E_2 ~ 208 nJ and an accessible lateral resolution of ~2 μm. At this energy, the crater diameter was evaluated to ~1.6 μm, which correspond to a fluence of 11 J.cm^{-2}. Note that the measured diameter is just twice as large as the theoretical spot diameter, estimated at 0.8 μm for this x50 magnification lens and for a perfect Gaussian beam emitting at 266 nm.

3.1.2. Plasma kinetics

The plasma formed under such low energy condition is low emissive and is approaching our detection limit. Therefore, it becomes crucial to characterize the temporal behavior of the plasma to optimize acquisition parameters (mainly the delay and gate). The experiments were conducted on the same type of aluminum as in the previous section. A temporal scan with an incremental delay of 20 ns and a gate of 20 ns was performed. Additionally, the study of the environment where the plasma is produced (air or argon) was also investigated for two laser energies (i.e. in the range of E_2 and E_5 respectively) allowing to achieve 2 and 3 μm lateral resolutions, respectively.

In Fig. 4, each point represents the accumulation of 200 spectra, and the recorded intensity corresponds to the integration of the aluminum line at 309.27 nm. As observed in this figure, the highest intensity value is obtained in argon environment with a delay of ~40 ns. Without argon, for the same laser energy, the maximum is obtained at ~60 ns. More importantly, as can be seen, the use of argon increases the collected signal by about a factor 2. Although in the low energy configuration, the optimal delay is 40 ns, the addition of argon still increases the sensitivity by about a factor 2. As expected, the plasma in argon, regardless of the configuration, lasts longer, here, for 80 ns. Furthermore, the plasma lifetime under argon is longer by 60 ns for the high energy configuration compared to the low energy configuration. These findings reveal that, as expected, the plasma powered by higher laser energy is better heated, increasing both the quantity of emitted photons and its lifetime. In air, this change is less pronounced, and no signal is obtained beyond 100 ns. All these observations made us conclude that it is mandatory to use argon for our experiments specially when we work with a low laser energy.

3.1.3. Imaging performances

Once all the technical and critical aspects related to the ablation process were understood, a first mapping experiment was performed on the aluminum standard. The obtained elemental images of Al, Cu, Mg, and Si are presented in Fig. 5. The laser energy was in the range of E_2. The sample was scanned over 1.3 mm along the horizontal and vertical axes, corresponding to a total of 292,500 pixels (laser shots). The analysis duration was ~4 h. As can be seen in Fig. 5, the sample contains silicon inclusions within the aluminum matrix. Inside these inclusions, no aluminum or magnesium is detected, and some copper is retained on certain inclusions. In this case, copper is rather evenly distributed across the analyzed area. The distribution of magnesium is subtler, with connected ridges visible in the lower part of the sample. Beyond this, magnesium is present significantly across the entire scanned surface. These ridges might potentially be indicative of sample contamination. Apart from the silicon inclusions, the distribution of silicon is complex and exhibits ordered patterns. These patterns resemble the geometric distribution observed in hypereutectic aluminum (with a silicon content greater than 12.6 %), as explained in [32].

Nevertheless, in the aluminum map shown in Fig. 5, streaks of aluminum distribution are observed. During analysis, the movement of the stage is not always perfectly repeatable, leading to slight jerks and causing observable streaks. To mitigate this non-chemical artifact, we may propose a normalization using the standard normal variate (SNV) method, which is well-suited for this case. The normalized images are shown in supplementary Fig. 2, and as can be seen we observe a significant improvement in the elemental image quality. Nevertheless, it remains essential to tailor this normalization technique to samples that permit it. In the case of a heterogeneous sample with a complex chemical composition and emission spectra that vary only slightly, SNV normalization may not be suitable. Its use would slightly smooth the elemental map intensities shot by shot, leading to a loss of relevant information about the sample. For these reasons, the analysis of lithium-ion battery electrodes should be conducted without such normalization.

3.2. Examples of battery imaging

3.2.1. Commercial battery internal stack

The analyzed sample is depicted in Fig. 1.a. The region corresponding to the LIBS images is outlined in Fig. 6.a. The scan size is 2 mm by 2 mm, equivalent to 1 million laser shots at a 2 μm lateral resolution.

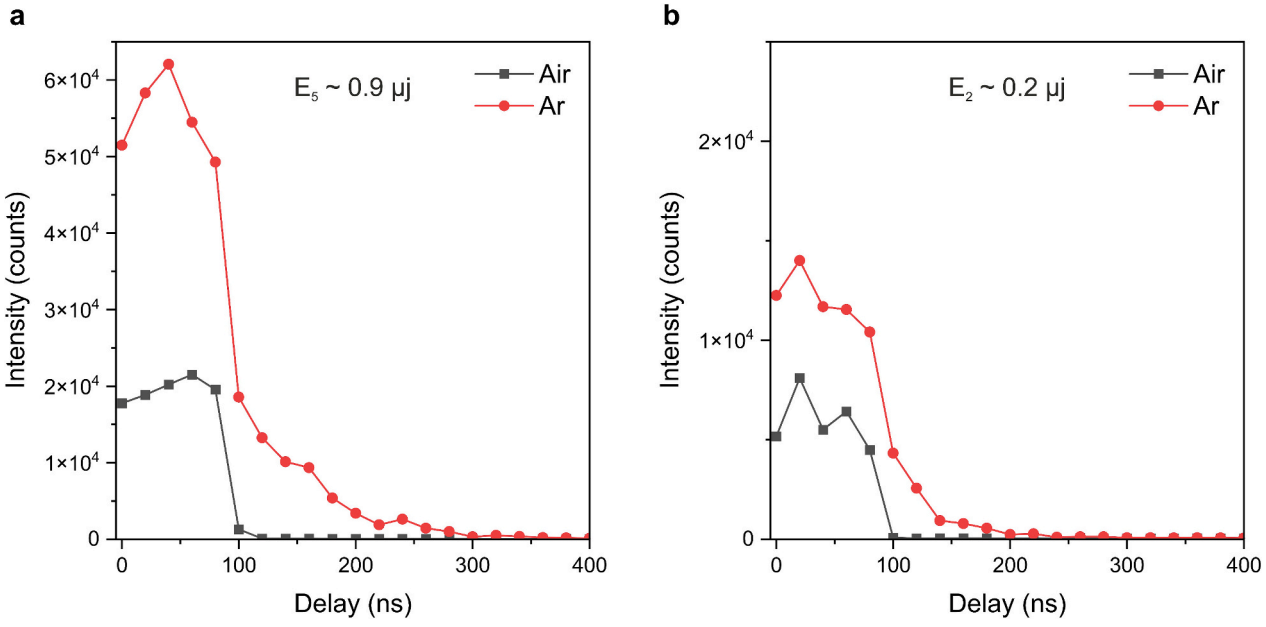

Fig. 4. (a) Evolution of the net intensity collected with a delay and gate step of 20 ns with two different plasma environment, argon and air at two laser energy, (a) E_5 and (b) E_2. The sample is the same type of aluminum used previously.

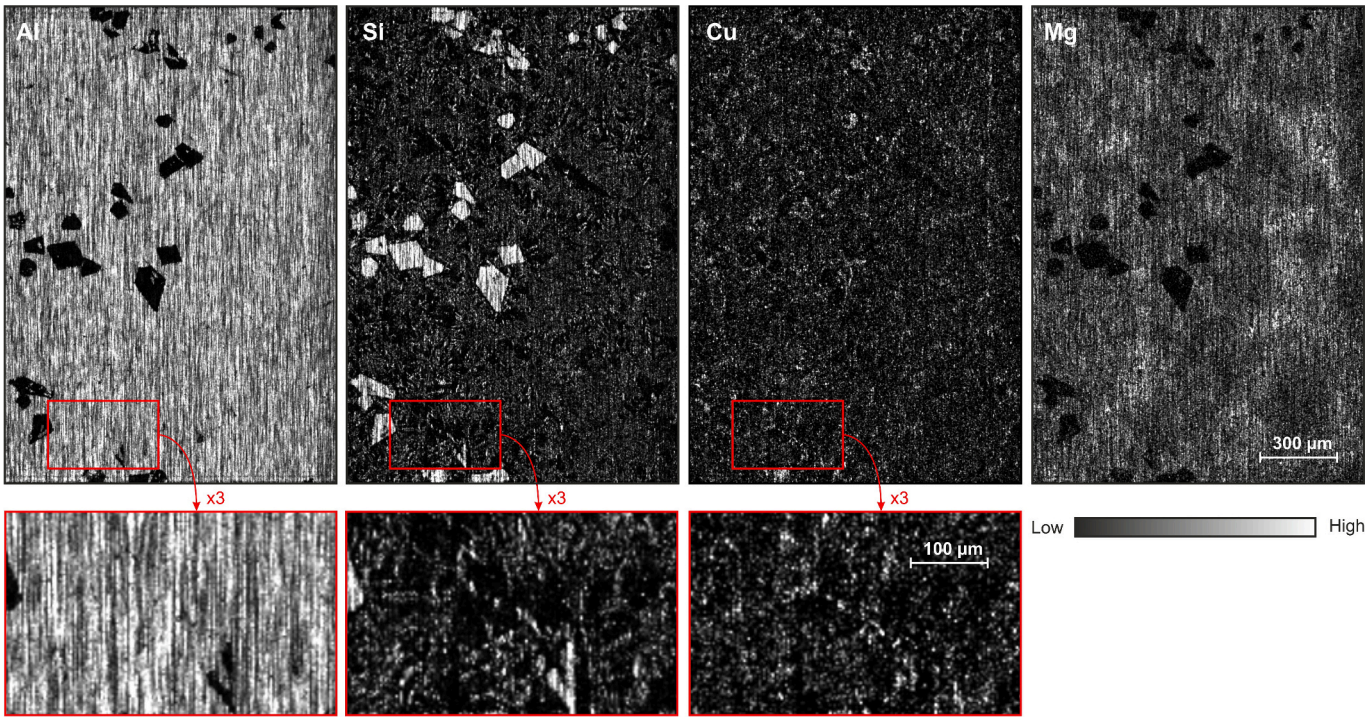

Fig. 5. Elemental maps of aluminum certified sample with a lateral resolution of 2 µm. The chemical distribution of Al, Si, Cu and Mg is shown.

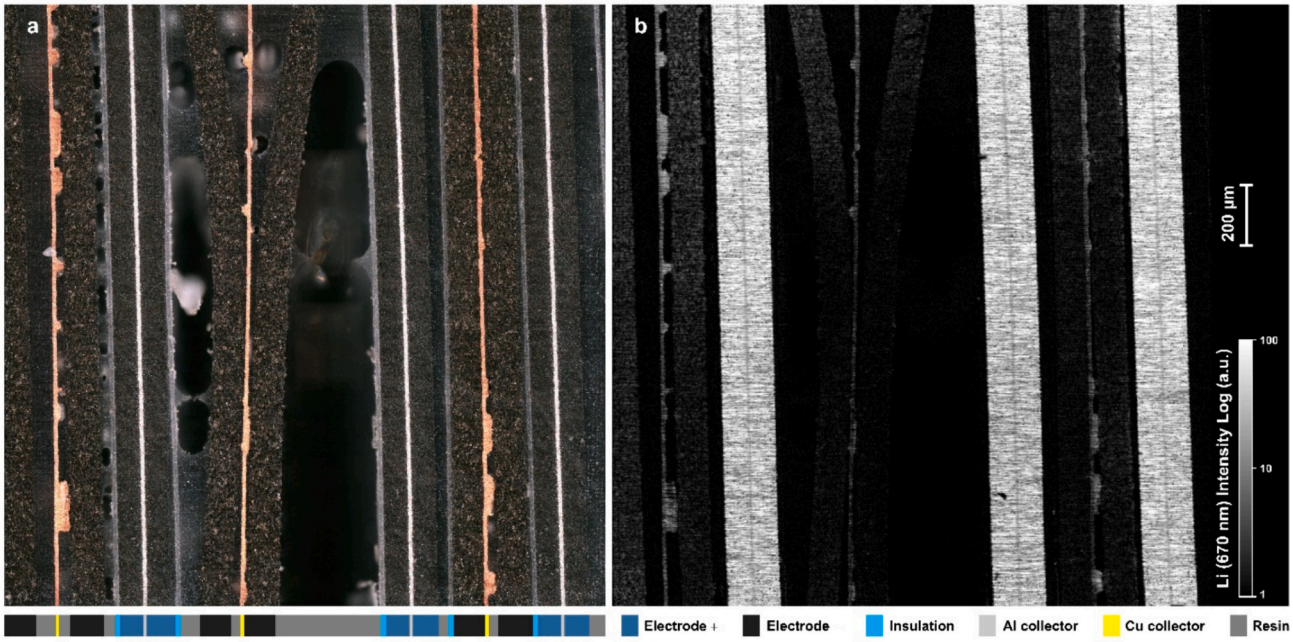

Fig. 6. (a) Optical image of the scanned sample. (b) Elemental image of lithium (Li 670.79 nm) at 2 µm lateral resolution. Positive (besides aluminum collectors) and negative electrodes (besides copper collectors) are respectively represented by a high and low signal of lithium.

This experiment required an analysis time of ~14 h. The LIBS lithium image obtained with the 670.79 nm line is represented in Fig. 6.b. Additionally, given the observed high intensity dynamic range, intensities were expressed on a logarithmic scale. This procedure has been previously employed and validated in the analysis of complex matrices, such as geological samples [33]. As the commercial battery was dismantled in the discharged state, the concentration of lithium is very high (around 6.6 %) in the positive electrodes compared to the negative electrodes (less than 1 %). Therefore, the representation of lithium distribution in the sample is nuanced. Please note that the concentrations of these two types of electrodes were obtained using ICP-AES.

Copper and aluminum collectors appear on both sides of their respective active materials, as can be seen in the optical image. A slight aluminum signal was observed (not shown here) at the separator level, attributed to the presence of a thin alumina coating on the separator's surface. However, on these same pixels containing aluminum, lithium was also present. Throughout the sample, we observe lithium into both copper and aluminum collectors. In the positive electrodes, lithium is

distributed rather homogeneously across the entire sample. Due to the high concentration of lithium, it is difficult to notice lithium distribution within the active material grains of the positive electrode. On the contrary, the lithium distribution is easily observable when examining the negative electrodes where the concentration of lithium is low. In an ideal scenario, no lithium detection should occur in the negative electrodes as the battery was dismantle in the discharged state but a substantial signal is obtained. Thus, a portion of the cyclable lithium crucial for the battery's proper functioning is trapped in the negative electrode highlighting the high benefit interest of high spatial resolution imaging. Since the battery's origin is commercial, the SEI layer is formed during the formation process of the battery. Thus, the lithium detected in the negative electrodes is very likely due to this process. We observe that the lithium distribution inside the negative electrode is not homogenous. This is particularly evident in the central negative electrode, gradually detaching from its copper collector (due to resin sample coating), where the lithium signal is weak at the upper part but intense at the lower part. Additionally, we observe lithium distribution within the active material grains of the graphite electrode. However, despite this information, determining the source of trapping, whether the growth of the solid electrolyte interface (SEI) or lithium plating predominates (in addition to other aging mechanisms), remains challenging. As we cannot clearly see dense concentration of lithium inside the negative electrode, we can assume that the formation process of the battery was controlled to reduce the lithium plating effect.

3.2.2. NMC 811 electrodes at different SoC

The elemental distribution of lithium, with a lateral resolution of 2 μm, is illustrated in Fig. 7. Please note that an adaptation of this figure, showing the distribution of lithium at a higher magnification, is available in Supplementary fig. 3. The elemental map encompasses a spatial dimension of 0.4 by 1.3 mm, consisting of 260,000 pixels at a lateral resolution of 2 μm. For the SoC 0 %, the lithium is intercalated in the positive electrode. For samples with SoC 0 and 50 %, the lithium distribution shows the electrode's structure with about 10 μm Li-rich round zone and porosity very similar to the active matter grains microstructure. For these electrodes, it is difficult to see isolated grains (from the electric percolation network) as the repartition of lithium is well distributed along the electrode. These observations seem to be not verified when we pay attention to the last sample (i.e. Fig. 7.c). If we look at the lithium distribution, we observe that the lithium signal along the left part of the electrodes is lower than the rest. Furthermore, we notice that few active matter grains have a high signal of lithium compared to others. It could possibly indicate that some active matter grains are isolated from the electric percolation network. Upon charging the battery, a reduction in lithium quantity within the positive electrode is observed, accompanied by a decrease in the number of active material grains exhibiting high lithium concentrations. This observed behavior aligns with the anticipated and inherent characteristics, validating the suitability of the device for lithium analysis within electrodes.

4. Conclusion

In this article, we propose an original micro-LIBS instrumentation, combining a high numerical aperture (0.42) microscope objective and a short laser wavelength (266 nm), enabling access to lateral measurement resolutions at the micrometer scale. This instrumentation, allows an ultimate resolution of ~2 μm to be achieved. At this resolution, sensitivity drastically decreases, presenting a challenge in further improving lateral resolution due to this constraint. Given the short lifespan of the formed plasma, precise control of the temporal window during acquisition is imperative. In this regard, and to optimize signal collection efficiency, all critical instrumental points are presented in detail. Various examples are shown on different types of materials (aluminum reference, battery electrodes) to assess the performance of this system for mapping. Several instrumental shortcomings, which will be corrected in a near future, have been identified, such as the long-term stability of the laser energy and the precision of the translation stages. However, these results demonstrate the full potential of this micro-LIBS instrument for analyzing lithium distribution in electrodes. The attainment of micrometric resolution in this study context indeed opens up broad perspectives for battery research, particularly in understanding aging mechanisms.

CRediT authorship contribution statement

Jordan Fernandes: Writing – review & editing, Writing – original draft, Visualization, Validation, Software, Methodology, Investigation, Formal analysis, Conceptualization. **Loïc Sorbier:** Writing – review & editing, Supervision, Project administration, Methodology, Funding acquisition, Conceptualization. **Sylvain Hermelin:** Writing – review & editing, Software, Investigation, Formal analysis, Conceptualization. **Jean-Michel Benoit:** Writing – review & editing, Resources, Formal analysis. **Christophe Dujardin:** Writing – review & editing,

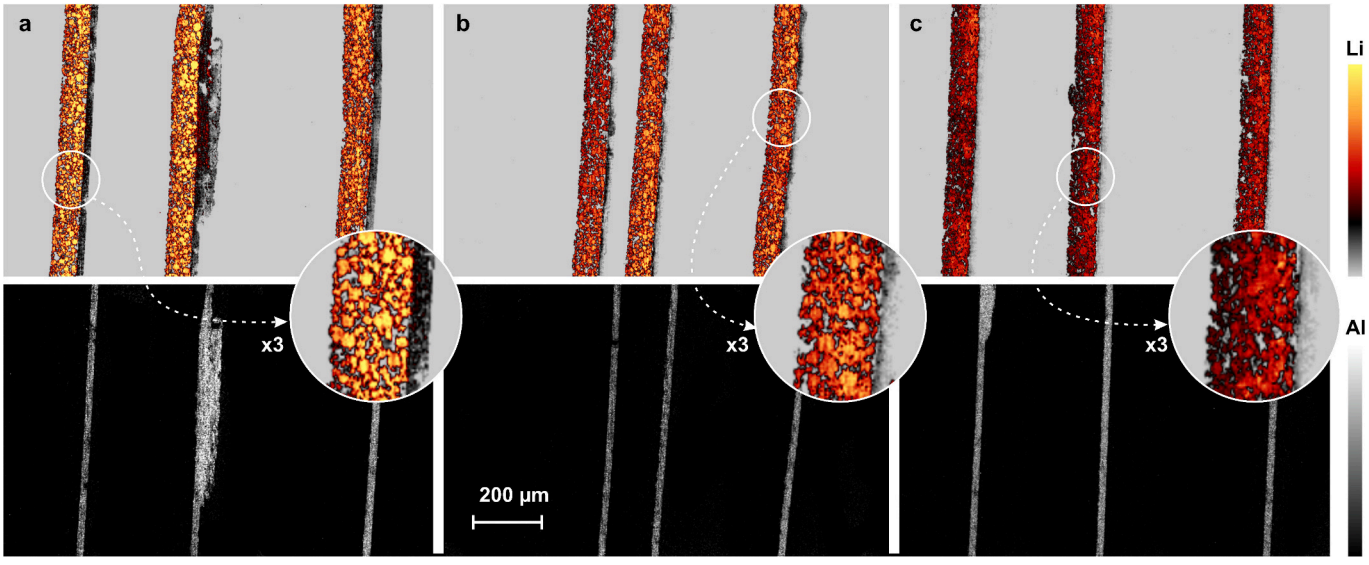

Fig. 7. NMC 811 electrode repartition of lithium and aluminum (grey color scale) with SoC of (a) 0 %, (b) 50 % and (c) 100 % with a lateral resolution of 2 μm. In each figure section a zoom at x3 magnification in the active matter region near the aluminum collector is also depicted.

Supervision, Project administration, Funding acquisition, Conceptualization. **Charles-Philippe Lienemann:** Writing – review & editing, Supervision, Methodology, Funding acquisition, Conceptualization. **Julien Bernard:** Writing – review & editing, Validation, Methodology, Investigation, Conceptualization. **Vincent Motto-Ros:** Writing – review & editing, Writing – original draft, Supervision, Software, Methodology, Funding acquisition, Conceptualization.

Declaration of competing interest

The authors declare that they have no known competing financial interests or personal relationships that could have appeared to influence the work reported in this paper.

The author is an Editorial Board Member/Editor-in-Chief/Associate Editor/Guest Editor for *[Journal name]* and was not involved in the editorial review or the decision to publish this article.

Data availability

Data will be made available on request.

Acknowledgments

This work was supported by the French "Agence Nationale de la Recherche" (ANR-20-CE05-0015 "Micro-Q-Li), and partially supported by the French region Rhônes Alpes Auvergne (Optolyse, CPER2016). The authors would also like to thank the CTMU for electron microscopy imaging, as well as Alan Guyon (ICP analysis and sample preparation) and Alexandre Gibert (battery cycling), both from IFPEN.

Appendix A. Supplementary data

Supplementary data to this article can be found online at https://doi.org/10.1016/j.sab.2024.107047.

References

[1] J.B. Goodenough, K.-S. Park, The li-ion rechargeable battery: a perspective, J. Am. Chem. Soc. 135 (2013) 1167–1176, https://doi.org/10.1021/ja3091438.
[2] I. Baccouche, S. Jemmali, B. Manai, A. Nikolian, N. Omar, N. Essoukri Ben Amara, Li-ion battery modeling and characterization: an experimental overview on NMC battery, Int. J. Energy Res. 46 (2022) 3843–3859.
[3] E. Peled, The electrochemical behavior of alkali and alkaline earth metals in nonaqueous battery systems—the solid electrolyte interphase model, J. Electrochem. Soc. 126 (1979) 2047–2051, https://doi.org/10.1149/1.2128859.
[4] H. Bryngelsson, M. Stjerndahl, T. Gustafsson, K. Edström, How dynamic is the SEI? J. Power Sources 174 (2007) 970–975, https://doi.org/10.1016/j.jpowsour.2007.06.050.
[5] P. Verma, P. Maire, P. Novák, A review of the features and analyses of the solid electrolyte interphase in li-ion batteries, Electrochim. Acta 55 (2010) 6332–6341, https://doi.org/10.1016/j.electacta.2010.05.072.
[6] J. Vetter, P. Novák, M.R. Wagner, C. Veit, K.-C. Möller, J.O. Besenhard, M. Winter, M. Wohlfahrt-Mehrens, C. Vogler, A. Hammouche, Ageing mechanisms in lithium-ion batteries, J. Power Sources 147 (2005) 269–281, https://doi.org/10.1016/j.jpowsour.2005.01.006.
[7] J. Groot, State-of-Health Estimation of Li-Ion Batteries: Cycle Life Test Methods, 2012.
[8] C.-H. Chen, F. Brosa Planella, K. O'Regan, D. Gastol, W.D. Widanage, E. Kendrick, Development of experimental techniques for parameterization of multi-scale Lithium-ion battery models, J. Electrochem. Soc. 167 (2020) 080534, https://doi.org/10.1149/1945-7111/ab9050.
[9] J. Newman, N. Balsara, Electrochemical Systems, 2021.
[10] C. Edouard, M. Petit, C. Forgez, J. Bernard, R. Revel, Parameter sensitivity analysis of a simplified electrochemical and thermal model for li-ion batteries aging, J. Power Sources 325 (2016) 482–494, https://doi.org/10.1016/j.jpowsour.2016.06.030.
[11] E. Prada, D. Di Domenico, Y. Creff, J. Bernard, V. Sauvant-Moynot, F. Huet, A simplified electrochemical and thermal aging model of LiFePO $_4$ -graphite li-ion batteries: power and capacity fade simulations, J. Electrochem. Soc. 160 (2013) A616–A628, https://doi.org/10.1149/2.053304jes.
[12] J.A. Österreicher, C. Simson, A. Großalber, S. Frank, S. Gneiger, Spatial lithium quantification by backscattered electron microscopy coupled with energy-dispersive X-ray spectroscopy, Scr. Mater. 194 (2021) 113664, https://doi.org/10.1016/j.scriptamat.2020.113664.
[13] S. Bessette, A. Paolella, C. Kim, W. Zhu, P. Hovington, R. Gauvin, K. Zaghib, Nanoscale Lithium quantification in LiXNiyCowMnZO2 as cathode for rechargeable batteries, Sci. Rep. 8 (2018) 17575, https://doi.org/10.1038/s41598-018-33608-3.
[14] P. Hovington, V. Timoshevskii, S. Burgess, H. Demers, P. Statham, R. Gauvin, K. Zaghib, Can we detect li K X-ray in lithium compounds using energy dispersive spectroscopy?: can we detect li K X-ray in lithium compounds using EDS? Scanning 38 (2016) 571–578, https://doi.org/10.1002/sca.21302.
[15] Z. Deng, X. Lin, Z. Huang, J. Meng, Y. Zhong, G. Ma, Y. Zhou, Y. Shen, H. Ding, Y. Huang, Recent Progress on advanced imaging techniques for Lithium-ion batteries, Adv. Energy Mater. 11 (2021) 2000806.
[16] P. Smyrek, T. Bergfeldt, H.J. Seifert, W. Pfleging, Laser-induced breakdown spectroscopy for the quantitative measurement of lithium concentration profiles in structured and unstructured electrodes, J. Mater. Chem. A 7 (2019) 5656–5665, https://doi.org/10.1039/C8TA10328C.
[17] S. Imashuku, H. Taguchi, T. Kawamata, S. Fujieda, S. Kashiwakura, S. Suzuki, K. Wagatsuma, Quantitative lithium mapping of lithium-ion battery cathode using laser-induced breakdown spectroscopy, J. Power Sources 399 (2018) 186–191, https://doi.org/10.1016/j.jpowsour.2018.07.088.
[18] S. Imashuku, H. Taguchi, S. Fujieda, S. Suzuki, K. Wagatsuma, Three-dimensional lithium mapping of graphite anode using laser-induced breakdown spectroscopy, Electrochim. Acta 293 (2019) 78–83, https://doi.org/10.1016/j.electacta.2018.10.013.
[19] Y. Zheng, L. Pfäffl, H.J. Seifert, W. Pfleging, Lithium distribution in structured graphite anodes investigated by laser-induced breakdown spectroscopy, Appl. Sci. 9 (2019) 4218, https://doi.org/10.3390/app9204218.
[20] H. Hou, L. Cheng, T. Richardson, G. Chen, M. Doeff, R. Zheng, R. Russo, V. Zorba, Three-dimensional elemental imaging of li-ion solid-state electrolytes using fs-laser induced breakdown spectroscopy (LIBS), J. Anal. At. Spectrom. 30 (2015) 2295–2302, https://doi.org/10.1039/C5JA00250H.
[21] V. Zorba, J. Syzdek, X. Mao, R.E. Russo, R. Kostecki, Ultrafast laser induced breakdown spectroscopy of electrode/electrolyte interfaces, Appl. Phys. Lett. 100 (2012) 234101, https://doi.org/10.1063/1.4724203.
[22] S.P. Banerjee, R. Fedosejevs, Single-shot ablation threshold of chromium using UV femtosecond laser pulses, Appl. Phys. A Mater. Sci. Process. 117 (2014) 1473–1478, https://doi.org/10.1007/s00339-014-8577-y.
[23] D.J. Hwang, H. Jeon, C.P. Grigoropoulos, J. Yoo, R.E. Russo, Femtosecond laser ablation induced plasma characteristics from submicron craters in thin metal film, Appl. Phys. Lett. 91 (2007) 251118, https://doi.org/10.1063/1.2825289.
[24] W. Wang, L. Sun, P. Zhang, L. Qi, L. Zheng, W. Dong, Microanalysis of molybdenum-copper stainless steel samples by picosecond laser-induced breakdown spectroscopy, Microchem. J. 158 (2020) 105267, https://doi.org/10.1016/j.microc.2020.105267.
[25] D. Menut, P. Fichet, J.-L. Lacour, A. Rivoallan, P. Mauchien, Micro-laser-induced breakdown spectroscopy technique: a powerful method for performing quantitative surface mapping on conductive and nonconductive samples, Appl. Opt. 42 (2003) 6063, https://doi.org/10.1364/AO.42.006063.
[26] R.E. Russo, X.L. Mao, O.V. Borisov, H. Liu, Influence of wavelength on fractionation in laser ablation ICP-MS, J. Anal. At. Spectrom. 15 (2000) 1115–1120, https://doi.org/10.1039/b004243i.
[27] J.-L. Lacour, N. Caron, K. Beranger, Device for The High-Resolution Mapping and Analysis of Elements in Solids, WO 20152/032024 A1, 2012.
[28] L. Sancey, V. Motto-Ros, B. Busser, S. Kotb, J.M. Benoit, A. Piednoir, F. Lux, O. Tillement, G. Panczer, J. Yu, Laser spectrometry for multi-elemental imaging of biological tissues, Sci. Rep. 4 (2014) 6065, https://doi.org/10.1038/srep06065.
[29] S. Moncayo, L. Duponchel, N. Mousavipak, G. Panczer, F. Trichard, B. Bousquet, F. Pelascini, V. Motto-Ros, Exploration of megapixel hyperspectral LIBS images using principal component analysis, J. Anal. At. Spectrom. 33 (2018) 210–220, https://doi.org/10.1039/C7JA00398F.
[30] V. Motto-Ros, S. Moncayo, F. Trichard, F. Pelascini, Investigation of signal extraction in the frame of laser induced breakdown spectroscopy imaging, Spectrochim. Acta B At. Spectrosc. 155 (2019) 127–133, https://doi.org/10.1016/j.sab.2019.04.004.
[31] G. Raciukaitis, Use of high repetition rate and high power lasers in microfabrication: how to keep the efficiency high? JLMN 4 (2009) 186–191, https://doi.org/10.2961/jlmn.2009.03.0008.
[32] M. Warmuzek, Aluminum-Silicon Casting Alloys: An Atlas of Microfractographs, ASM International, 2004.
[33] C. Fabre, D. Devismes, S. Moncayo, F. Pelascini, F. Trichard, A. Lecomte, B. Bousquet, J. Cauzid, V. Motto-Ros, Elemental imaging by laser-induced breakdown spectroscopy for the geological characterization of minerals, J. Anal. At. Spectrom. 33 (2018) 1345–1353, https://doi.org/10.1039/C8JA00048D.